Computational Physics II - Exercise 6, Group 14
Electrostatics in a cylinder with variable dielectric and free charges

Ian LE MEUR Xavier KERVYN
ian.lemeur@epfl.ch xavier.kervyn@epfl.ch

13th April 2021

1 Introduction

This exercise aims to study the equation governing the electric potential in electrostatics, which is a second order spatially dependent partial differential equation. This problem will be treated using the finite element method, to transform it into a variational form, which will then be discretized, using Galerkin's method, leading to a linear algebraic system. Numerically, the points of interest will be the prioritization of different spatial intervals, as well as the study of numerical errors which occur due to physical discontinuities. Physically, a focus will be given to the study of the electric potential that ensues from a given charge distribution, as well as the discontinuities that result from a change in electric permitivitty. A verification of Gauss' law will be undertaken and the bound charges in a given configuration will be found, both analytically and numerically.

2 Analytic calculations

We now aim to derive the differential equations modelising the spatial variation of the electric potential ϕ in matter. We use Gauss' law for the displacement field $\vec{D}$, as well as the expression for the electric field $\vec{E}$ with respect to the scalar and magnetic potentials, and finally the constitutive relation for the displacement field in a linear dielectric:

$$\nabla \cdot \vec{D} = \rho_f \,, \quad \vec{E} = -\nabla\phi - \frac{\partial \vec{A}}{\partial t} \,, \quad \vec{D} = \varepsilon_0 \varepsilon_r \vec{E} \,, \tag{1}$$

with ρ_f the free charge density, $\vec{A}$ the magnetic potential, ε_0 the permittivity of free space and ε_r the relative permittivity of the medium. In the static case the time derivative of $\vec{A}$ vanishes, and one thus obtains the following differential equation for a charge configuration in a volume Ω (considered as an open topological subset of $\mathbb{R}^n$):

$$\nabla \cdot (\varepsilon_0 \varepsilon_r(\vec{x}) \nabla\phi(\vec{x})) = \rho_f(\vec{x}) \,, \forall \vec{x} \in \Omega \,, \quad \phi(\vec{x}) = V(\vec{x}) \,, \forall \vec{x} \in \partial\Omega \,, \tag{2}$$

with V a given potential at the boundary of the volume $\partial\Omega$. In order to solve this problem numerically, we convert the problem (2) into its variational form, by multiplying the differential equation by a test function $\eta \in C^1(\Omega)$, chosen such that $\eta(\vec{x}) = 0 \,, \forall \vec{x} \in \partial\Omega$. We then

integrate this relation over the domain Ω to obtain

$$\int_\Omega \eta \nabla \cdot (\varepsilon_r \nabla \phi) \mathrm{d}\vec{x} = -\int_\Omega \eta \frac{\rho_f}{\varepsilon_0} \mathrm{d}\vec{x}\,. \tag{3}$$

Using the product rule $\eta \nabla \cdot (\varepsilon_r \nabla \phi) = \nabla \cdot (\eta \varepsilon_r \nabla \phi) - \varepsilon_r \nabla \eta \cdot \nabla \phi$, and the divergence theorem, one obtains

$$\int_\Omega \eta \nabla \cdot (\varepsilon_r \nabla \phi) \mathrm{d}\vec{x} = \int_{\partial\Omega} \eta \varepsilon_r \nabla \phi \mathrm{d}\sigma - \int_\Omega \varepsilon_r \nabla \eta \cdot \nabla \phi \mathrm{d}\vec{x}\,, \tag{4}$$

where the first term on the right hand side is zero thanks to the condition $\eta(\vec{x}) = 0\,, \forall \vec{x} \in \partial\Omega$. The variational problem thus becomes

$$\int_\Omega \varepsilon_r \nabla \eta \cdot \nabla \phi \mathrm{d}\vec{x} = \int_\Omega \eta \frac{\rho_f}{\varepsilon_0} \mathrm{d}\vec{x}\,. \tag{5}$$

Due to the cylindrical symmetry of the problem (i.e. the radial dependence of ϕ, ε_r and ρ_f), the integrals can be explicitly written as

$$\int_0^{L_z} \mathrm{d}z \int_0^{2\pi} \mathrm{d}\theta \int_0^R r \varepsilon_r(r) \frac{\mathrm{d}\eta(r)}{\mathrm{d}r} \frac{\mathrm{d}\phi(r)}{\mathrm{d}r} \mathrm{d}r = \int_0^{L_z} \mathrm{d}z \int_0^{2\pi} \mathrm{d}\theta \int_0^R r \eta(r) \frac{\rho_f(r)}{\varepsilon_0} \mathrm{d}r\,, \tag{6}$$

with L_z and R the length and radius of the cylinder respectively. This expression can finally be simplified to

$$\int_0^R r \varepsilon_r(r) \frac{\mathrm{d}\eta(r)}{\mathrm{d}r} \frac{\mathrm{d}\phi(r)}{\mathrm{d}r} \mathrm{d}r = \int_0^R r \eta(r) \frac{\rho_f(r)}{\varepsilon_0} \mathrm{d}r\,. \tag{7}$$

To discretize this problem, the Galerkin method is used. The latter consists in using a basis

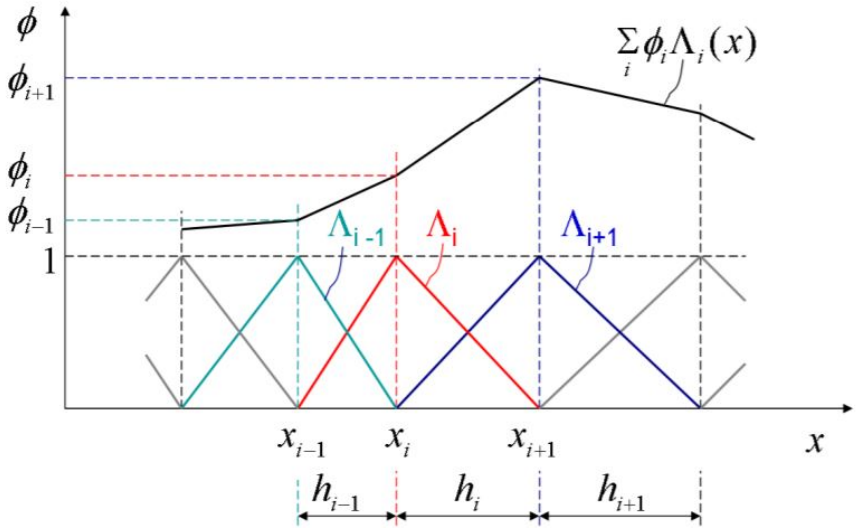

Figure 1: Illustration of the Galerkin discretization method described in the text [1].

of piecewise differentiable functions denoted by Λ_i, equal to 1 at r_i and 0 at r_j for $j \neq i$, where the r_i are a set of points in the interval $[0, R]$ that are not necessarily equidistant from one another, as represented in Figure 1. This approximation leads to

$$\phi(r) \approx \sum_i \phi_i \lambda_i(r) \quad \eta(r) \approx \sum_i \eta_i \lambda_i(r), \tag{8}$$

and it can be shown that as i tends to infinity, the approximation becomes an equality. Substituting equation (8) into (7) yields

$$\sum_i \eta_i \sum_j \left(\int_0^R r\varepsilon_r \frac{\mathrm{d}\Lambda_i}{\mathrm{d}r} \frac{\mathrm{d}\Lambda_j}{\mathrm{d}r} \mathrm{d}r \right) \phi_j = \sum_i \eta_i \left(\int_0^R r\Lambda_i \frac{\rho_f}{\varepsilon_0} \mathrm{d}r \right) , \tag{9}$$

As this equation is valid for all η_i, the outer sums can be simplified, leading to the matrix equation:

$$A_{i,j}\phi_j = b_i \, . \tag{10}$$

The integrals can be approximated using a formula that combines the trapezoid and midway point methods:

$$\int_{r_k}^{r_{k+1}} f(r)\mathrm{d}r \approx h_k \left[p\frac{f(r_k) + f(r_{k+1})}{2} + (1-p) f\left(r_{k,mid}\right) \right] , \tag{11}$$

with $h_k = r_{k+1} - r_k$ the step size, $r_{k,mid} = (r_k + r_{k+1})/2$ the midpoint and $0 \leq p \leq 1$ a parameter that can be used to vary the method of approximation ($p = 0$ gives the midway point method, whereas $p = 1$ gives the trapezoidal method). This gives the required numerical approximations for the matrix elements:

$$A_{k,k} = \frac{1}{2h_k} \left[p(r_k\varepsilon_r(r_k) + r_{k+1}\varepsilon_r(r_{k+1})) + (1-p)(r_k + r_{k+1})\varepsilon_r\left(r_{k,mid}\right) \right] , \tag{12}$$

$$A_{k,k+1} = -\frac{1}{2h_{k+1}} \left[p(r_k\varepsilon_r(r_k) + r_{k+1}\varepsilon_r(r_{k+1})) + (1-p)(r_k + r_{k+1})\varepsilon_r\left(r_{k,mid}\right) \right] , \tag{13}$$

with $A_{k,k+1} = A_{k+1,k}$, as well as the right hand side:

$$b_k = \frac{h_k}{4\varepsilon_0} \left[2pr_k\rho_f(r_k) + (1-p)(r_k + r_{k+1})\rho_f\left(r_{k,mid}\right) \right] . \tag{14}$$

The boundary conditions for $V(r = R) = V_0$ are then imposed by

$$A_{N,N-1} = 0 \quad A_{N,N} = 1 \quad b_N = V_0 \, , \tag{15}$$

with N the number of points in our discretized system. It is important to note that without these boundary conditions, the matrix associated to the system of equations is singular. To be able to solve the matrix equation (10), a Gauss-Jordan elimination method is used. To be able to compute the radial components of the electric field and electric displacement field, E_r and D_r, given the scalar potential, we use a finite difference method centred at the midpoints:

$$E_r(r_{k,mid}) = -\frac{\partial\phi}{\partial r}(r_{k,mid}) \approx -\frac{\phi(r_{k+1}) - \phi(r_k)}{r_{k+1} - r_k} \, , \tag{16}$$

$$D_r(r_{k,mid}) \approx \varepsilon_0\varepsilon_r(r_{k,mid})E_r(r_{k,mid}) \, . \tag{17}$$

We now aim to compute the divergence of these fields at the midpoints of the intervals $[r_{k-1/2}, r_{k+1/2}]$, we thus define the point $r_{k,midmid} = (r_{k,mid} + r_{k+1,mid})/2$ and use it to approximate the $\nabla \cdot \vec{E}$ in cylindrical coordinates:

$$\nabla \cdot \vec{E}(r_{k,midmid}) = \frac{1}{r}\frac{\partial(rE_r)}{\partial r}(r_{k,midmid}) \approx \frac{E_r(r_{k+1,mid})r_{k+1,mid} - E_r(r_{k,mid})r_{k,mid}}{r_{k,midmid} \cdot (r_{k+1,mid} - r_{k,mid})} \, , \tag{18}$$

$$\nabla \cdot \vec{D}(r_{k,midmid}) = \frac{1}{r}\frac{\partial(rD_r)}{\partial r}(r_{k,midmid}) \approx \frac{D_r(r_{k+1,mid})r_{k+1,mid} - D_r(r_{k,mid})r_{k,mid}}{r_{k,midmid} \cdot (r_{k+1,mid} - r_{k,mid})} \, . \tag{19}$$

3 Numerical simulations

3.1 Trivial case

In this section, we verify the validity and the consistency of the equations obtained above by considering a trivial case, that does not represent any physical situation but is straightforward to check. Recall that the problem consists of a "vacuum cylinder" of radius $b = 0.3$ m surrounded by a coaxial electrically neutral cylindrical shell of radii b and $R = 0.5$ m (width $R - b$). The outer shell is set at potential $V_0 = 220$ at $r = R$ initially. We solve equation (2) while supposing $\rho_f(r) = \varepsilon_0$ and $\varepsilon_r(r) = 1$. The problem now reads:

$$\nabla^2 \phi = -1\,, \tag{20}$$

The Laplacian operator in cylindrical coordinates reduces to

$$\begin{aligned} \frac{1}{r}\frac{\mathrm{d}}{\mathrm{d}r}\left(r\frac{\mathrm{d}\phi}{\mathrm{d}r}\right) = -1 \implies \frac{\mathrm{d}}{\mathrm{d}r}\left(r\frac{\mathrm{d}\phi}{\mathrm{d}r}\right) = -r \implies r\frac{\mathrm{d}\phi}{\mathrm{d}r} = -\frac{r^2}{2} + C_1 \\ \implies \frac{\mathrm{d}\phi}{\mathrm{d}r} = -\frac{r}{2} + \frac{c_1}{r} \implies \phi(r) = -\frac{r^2}{4} + C_1 \ln r + C_2\,. \end{aligned} \tag{21}$$

To determine the constants C_1 and C_2, we impose the condition that $\phi(0) < \infty$, yielding $C_1 = 0$, followed by $\phi(R) = V_0$, which finally gives

$$\phi(r) = \frac{R^2 - r^2}{4} + V_0. \tag{22}$$

To numerically solve the problem, the intervals $[0, b[$ and $[b, R]$ have been discretised in evenly-spaced steps. This is done by imposing a number of steps N to both intervals. The spacing h between two steps then corresponds to

$$h(r) = \begin{cases} b/N & \text{if } 0 \leq r < b \\ (R-b)/N & \text{if } b \leq r \leq R \end{cases}\,. \tag{23}$$

A first check of the validity of the equations is given in Figure 2 for the potential ϕ, where the latter is plotted as a function of the radius r, for different number of steps N ranging from 10 to 3360 steps. As expected, there is no discontinuity at $r = b$ and all simulations converge towards the initial value $V_0 = 220$ V as r approaches $R = 0.5$ m. Moreover, it appears that the simulations conducted also tend towards the analytical solution ϕ_{ana} obtained in (22), which is plotted in the red dashed line in the figure. So far, one can thus consider the equations to be qualitatively verified by the numerical simulation.

This was quantitatively assessed by a convergence study on the value of the potential ϕ at $r = 0$, that is to say at the center of the inner cylinder.

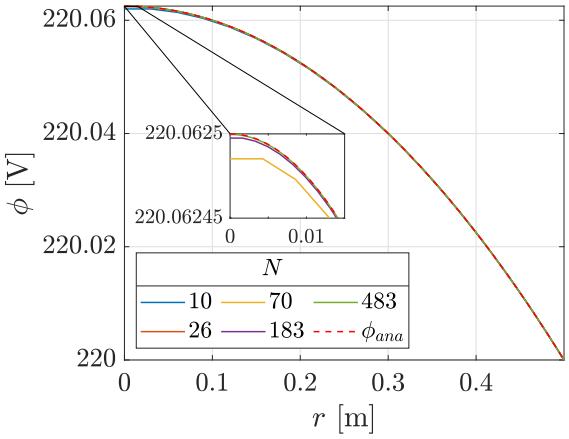

Figure 2: Simulations for the potential ϕ obtained for the trivial case, with $N = 30$ steps.

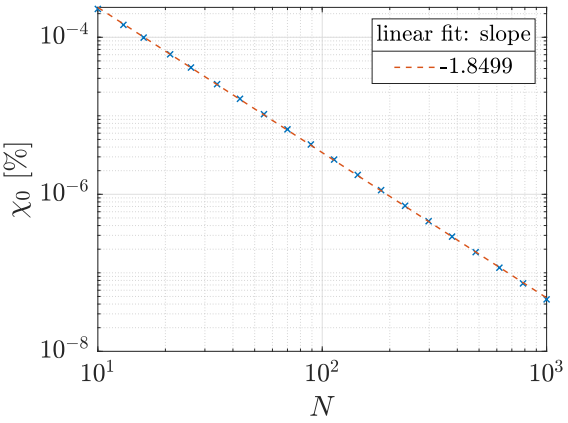

Figure 3: Convergence study on the potential $\phi(0)$ at $r = 0$ for 20 simulations with N ranging from 10 to 10^4 steps.

This can be done by plotting on a logarithmic-logarithmic plot the relative error on $\phi(0)$ against the analytic value obtained from (22), as a function of the number of steps taken N. The result of this undertaking can be seen in Figure 3. The slope of the linear best fit line plotted yields the order of convergence achieved by the simulation, which is in our case of approximately 2. This means that doubling the number of steps taken in the simulation consists in dividing by four the error obtained at $r = 0$. It can be shown analytically that the order of convergence of a numerical method that uses Galerkin functions increases as the degree of the basis polynomials Λ_i increases.

3.2 Non-trivial case

Having numerically verified the results obtained in the first part of this report, we now consider the problem in a more realistic and non-trivial approach. The relative permittivity of the outer shell ε_r varies. The symmetry of the system induces a dependence of the latter only on the radius r from the center of the inner cylinder. This relationship is given by the formula

$$\varepsilon_r(r) = \begin{cases} 1 & \text{if } 0 \leq r < b \\ 4 & \text{if } b \leq r \leq R \end{cases}, \qquad (24)$$

with $b = 0.3$ m the radius of the inner cylinder, that thus now represents a point of discontinuity in the equations involving ε_r and its derivatives. As the outer shell is supposed electrically neutral, there are no free charges on it. The free charge density ρ_f is set to an expression of the form

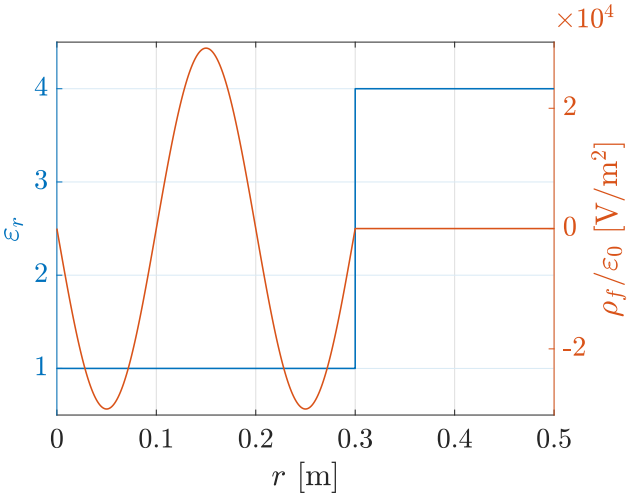

Figure 4: Relative permittivity ε_r and free charges density ρ_f/ε_0 profiles.

$$\rho_f(r)/\varepsilon_0 = \begin{cases} a_0 \sin\left(\frac{3\pi r}{b}\right) & \text{if } 0 \leq r < b \\ 0 & \text{if } b \leq r \leq R \end{cases}, \qquad (25)$$

with $a_0 = -3 \times 10^4$ V/m^2 and ε_0 the permittivity of free space. The exterior of the outer shell is again initially set at a potential $V_0 = 220$ V. The graphs of each of these variables are shown in Figure 4. It can be seen that the relative permittivity ε_r is discontinuous and the free charge density ρ_f is not differentiable at $r = b$. The resulting effects on the electric potential, as well as the electric field and electric displacement field, will thus be studied further on.

In fact, one can find an analytic solution for the electric potential ϕ in this configuration. Considering the cylindrical geometry of the system (under the approximation of a long cylinder), ϕ depends only on the radial distance from the axis r and one can compute $\phi(r)$ by calculating the line integral of $\vec{E}$:

$$\phi(r) = V_0 - \int_R^r E_r(s)\mathrm{d}s \tag{26}$$

with $V_0 = \phi(R)$ the boundary condition. The integral must be computed in two different cases $r < b$ and $r \geq b$, to treat the piecewise definition of both the free charge and the relative permitivitty on these intervals.

To compute the integral, one can use the integral form of Gauss' law applied to the electric displacement, and from this deduce the electric field. By integrating on a cylindrical Gaussian surface of radius r and length L_z, Gauss' law takes the following form:

$$\int_S \vec{D} \cdot \mathrm{d}\vec{S} = \int_V \rho_f \mathrm{d}V = Q_f \,, \tag{27}$$

Using the symmetry of the system one can notice that the magnitude of the displacement field is constant on the surface S. Thus, equation (27) can be rewritten as

$$2\pi L_z r D_r(r) = Q_f \,. \tag{28}$$

The computation of Q_f depends on r. If $r \geq b$, the total free charges contained in the volume are all the charges contained in the cylinder of radius b. Thus,

$$Q_{f,tot} = \varepsilon_0 a_0 2\pi L_z \int_0^b s \sin\left(\frac{3\pi}{b}s\right) \mathrm{d}s = \frac{2}{3} L_z a_0 \varepsilon_0 b^2 \,. \tag{29}$$

By injecting $Q_{f,tot}$ in equation (28), one can find an expression for D_r:

$$D_r(r) = \frac{a_0 \varepsilon_0 b^2}{3\pi r}, \tag{30}$$

and consequently find the electric field

$$E_r(r) = \frac{a_0 b^2}{12\pi r} \,. \tag{31}$$

If $r < b$, the total free charges contained in the volume of integration is obtained by integrating ρ_f in a cylinder of radius r. Hence, Q_f takes the following form:

$$Q_f = \frac{2 L_z a_0 \varepsilon_0 b^2}{9\pi} \left(\sin\left(\frac{3\pi}{b}r\right) - \frac{3\pi}{b} r \cos\left(\frac{3\pi}{b}r\right) \right) \,, \tag{32}$$

which gives an explicit expression for D_r by using equation (28):

$$D_r(r) = \frac{a_0 \varepsilon_0 b^2}{9\pi^2} \left(\frac{\sin\left(\frac{3\pi}{b} r\right)}{r} - \frac{3\pi}{b} \cos\left(\frac{3\pi}{b} r\right) \right) , \tag{33}$$

and E_r:

$$E_r(r) = \frac{a_0 b^2}{9\pi^2} \left(\frac{\sin\left(\frac{3\pi}{b} r\right)}{r} - \frac{3\pi}{b} \cos\left(\frac{3\pi}{b} r\right) \right) . \tag{34}$$

Since the expression of E_r has been found, it is possible to compute the electric potential by using equation (26). In the case $r \geq b$, one obtains

$$\phi(r) = V_0 - \frac{a_0 b^2}{12\pi} \ln\left(\frac{r}{R}\right) . \tag{35}$$

In the case $r < b$, one obtains

$$\phi(r) = V_0 - \frac{a_0 b^2}{9\pi^2} \left[\frac{3\pi}{4} \ln\left(\frac{b}{R}\right) + \int_b^r \frac{\sin\left(\frac{3\pi}{b} s\right)}{s} \mathrm{d}s - \sin\left(\frac{3\pi}{b} r\right) \right] . \tag{36}$$

One can also calculate the bound charge density ρ_b within the volume, using equation (2) and

$$\rho = \rho_b + \rho_f \, , \quad \nabla \cdot \vec{E} = \frac{\rho}{\varepsilon_0} \, , \tag{37}$$

one deduces

$$\rho_b = \varepsilon_0 \nabla \cdot (\varepsilon_r \nabla \phi + \vec{E}) \, . \tag{38}$$

When $r < b$, $\varepsilon_r = 1$ and thus the term within the parenthesis is zero by definition of the electric potential. When $r > b$, $\varepsilon = 4$ and thus the term in paranthesis is proportional to the divergence of the electric field, with $\vec{E}$ given by equation (31), yet a simple calculation yields

$$\nabla \cdot \vec{E} = \frac{1}{r} \frac{\partial}{\partial r} (r E_r) = \frac{1}{r} \frac{\partial}{\partial r} \left(\frac{a_0 b^2}{12\pi} \right) = 0 \, , \tag{39}$$

and thus one can conclude that the bound charge density ρ_b is always zero, except possibly at $r = b$, where there is a physical discontinuity: $\rho_b(r \neq b) = 0$. One can also calculate the total charge Q_{tot} using Gauss' law over the whole cylinder

$$\int_S \vec{E} \cdot \mathrm{d}\vec{S} = \int_0^{2\pi} \int_0^{L_z} \frac{a_0 b^2}{12\pi R} R \mathrm{d}z \mathrm{d}\theta = \frac{1}{6} a_0 b^2 L_z = \frac{1}{\varepsilon_0} Q_{tot} \, , \tag{40}$$

which then allows, using equation (29), one to find the total bound charge $Q_{b,tot}$, which is actually at the surface interface between the two different materials, i.e. at $r = b$:

$$Q_{b,tot} = Q_{tot} - Q_{f,tot} = -\frac{1}{2} \varepsilon_0 a_0 b^2 L_z \, . \tag{41}$$

These analytic results will be discussed later. For various values of $N_{tot} = N_1 + N_2$, the total number of intervals, the numerical simulation is executed. To understand the relative

importance between N_1 and N_2, the simulations are carried out in one case with $N_1 = kN_2$, and inversely in the case $N_1 = N_2/k$. The results of this study are shown in Figure 5.

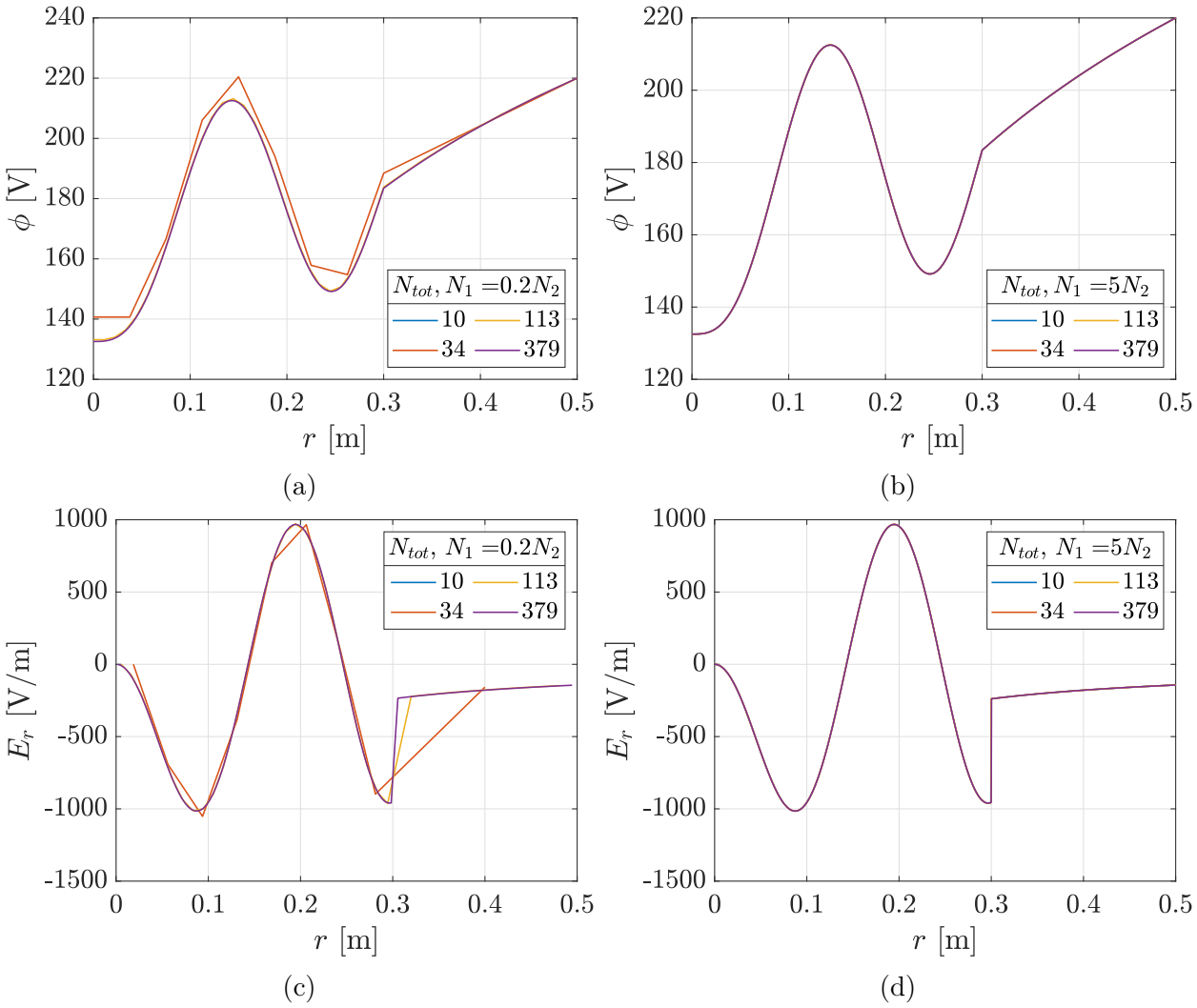

Figure 5: Comparative study of the impact of N_1 versus N_2, for (a & b) the potential ϕ; (c & d) the electric field E_r. Graphs for (a) and (c) (resp. (b) and (d)) were obtained for fixed values of N_{total} and $N1 = 0.2N_2$ (resp. $N_1 = 5N_2$).

It can be seen qualitatively that the convergence is more rapid in the case where N_1 is prioritised over N_2 (i.e. with $k > 1$), and this is to be expected, as the free charge density ρ_f is more complex in the region $0 < r < b$, and thus a more finely discretised grid in this section (corresponding to a larger N_1) is advantageous.

Potential at r=b Recall that an analytic value of the potential ϕ at $r = b$ can either be obtained from (35) or (36). Using the parameters mentioned above, one gets $\phi_{ana}(r = b) \approx 183.4148$ V. This value can be used to carry out quantitative studies on the simulation. With this in mind, simulations were conducted with 400 different pairs (N_1,N_2), with N_1, $N_2 \in [100, 1000]$. For each set out the 400 pairs, the relative error to the analytical solution at $r = b$ has been computed. The result of this undertaking can be seen in Figure 6.

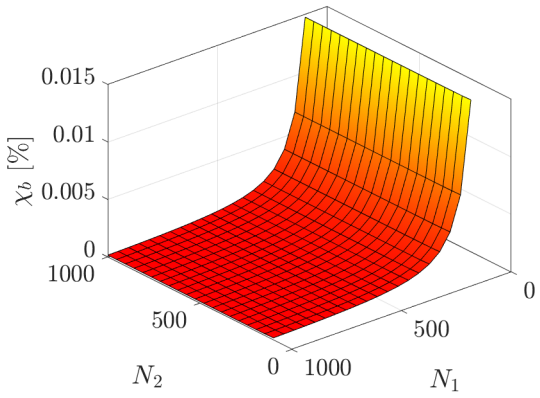

Figure 6: Surface plot of the relative error on the analytic value of the potential $\phi_{ana}(r = b)$, obtained with 400 different pairs $(N_1, N_2) \in [100, 1000] \times [100, 1000]$.

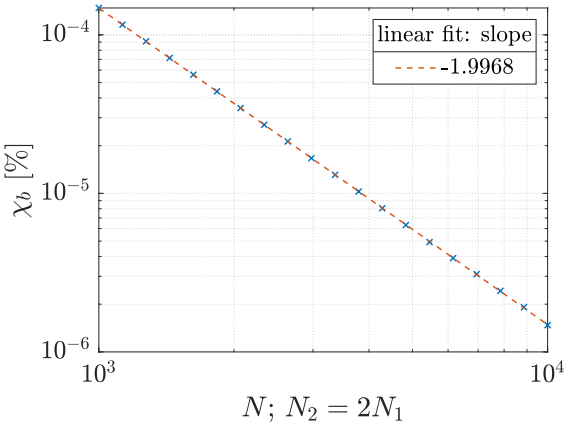

Figure 7: Convergence study of the analytic solution for the potential $\phi_{ana}(r = b)$, obtained with 20 simulations with $N = N_1$ ranging from 10^3 to 10^4 steps.

One can clearly see that an increase in the number of steps N_2 taken in the region where $r \geq b$ seems to have no or low impact on the relative error obtained at $r = b$, whereas the latter decreases as the number of steps N_1 taken in the region where $r < b$ increases. This is in concordance with the results shown in Figure 5. A convergence study on the value $\phi_{ana}(r = b)$ was carried out with 20 different values of $N_1 \in [10^3, 10^4]$ and a mesh factor of 2, i.e. $N_2 = 2N_1$. It can be seen in Figure 7, where the relative error on the analytic solution for ϕ at $r = b$, noted by

$$\chi_b = \left| \frac{\phi_{ana}(r = b) - \phi_{num}(r = b)}{\phi_{ana}(r = b)} \right| \times 100\,, \tag{42}$$

is plotted against increasing values of $N = N_1$ on a logarithmic-logarithmic scale. The order of convergence achieved by the simulation is once again given by the slope of the linear best fit line plotted, and one can see that it is again of approximately 2 as in Figure 3. This seems to be coherent with the profiles observed in 6, as the relative error on $\phi_{ana}(r = b)$ seems to decrease as $1/x^2$ when the number of steps N_1 increases.

Potential over the whole domain As equations (35) and (36) give a complete and continuous analytic solution for the potential over all the domain $0 \leq r \leq R$, the results obtained numerically for ϕ could also be studied at $r \neq b$. In Figure 8a, various potential profiles can be observed, as well as the aforementioned analytic solution. This provides a qualitative comparison between the outcomes of the simulations for different values of N_1 and the analytic solution. As expected, one can see that the potential tends towards the analytic solution as the simulation becomes more precise, i.e. as the number of steps taken increases.

To quantitatively show the magnitude of the relative error on the analytic solution, noted

$$\chi_a = \left| \frac{\phi_{ana}(r) - \phi_{num}(r)}{\phi_{ana}(r)} \right| \times 100\,, \tag{43}$$

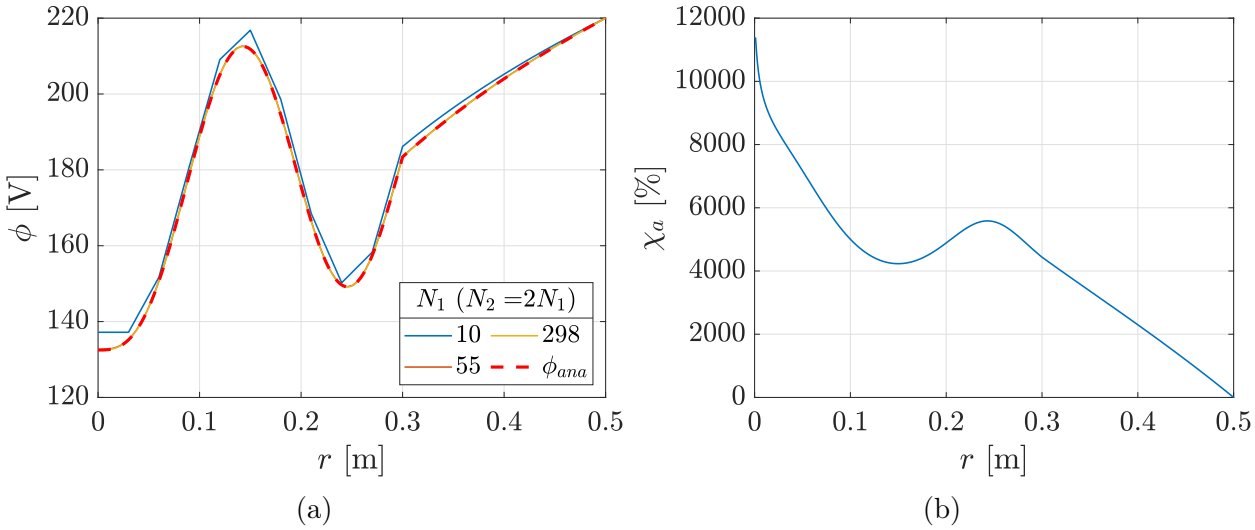

Figure 8: Potential over the whole domain. (a) Qualitative comparison between the analytical solution and the outcomes of various simulations; (b) Relative error to the analytical solution over the whole domain, obtained for a simulation conducted with $N_1 = 1000$ steps and a mesh factor of 2 (i.e. $N_2 = 2N_1$).

over the course of the simulation, the relative error is plotted in Figure 8b. It corresponds to a simulation conducted with $N_1 = 1000$ steps and a mesh factor of 2. One can see that it reaches its maximal value of approximately $4 \times 10^{-3}\%$ at $r = 0$ and then oscillates and decreases towards 0%. This further ascertains the validity of the analytic solution.

Verification of Gauss' Law We now proceed to a verification of Gauss' law in differential form for the electric displacement field, i.e. $\nabla \cdot \vec{D} = \rho_f$. Here, the divergence is calculated using the finite difference formula given in equation (19). To achieve this, the absolute value of $(\nabla \cdot \vec{D} - \rho_f)/a_0$ was analysed for various simulations with different numbers of intervals N. This difference represents an error on the divergence of the electric displacement, and has been divided by a_0 in order to be able to consider a relative error. We note

$$\chi_d = \left| \frac{\nabla \cdot \vec{D} - \rho_f}{a_0} \right| \times 100 \tag{44}$$

this relative error. This is shown in Figure 9a.

It can be seen that the error is close to zero everywhere, except in a small neighbourhood around $r = b$ where the error peaks. However, it can be seen that the height of the peak diminishes as the number of intervals N augments. This implies that this peak is numerical in nature. To confirm this, a convergence study was conducted on the peak value of the error, and this is shown in Figure 9b, where the maximum of the relative error on $\nabla \cdot \vec{D}$ is plotted against $1/N$ on a linear scale.

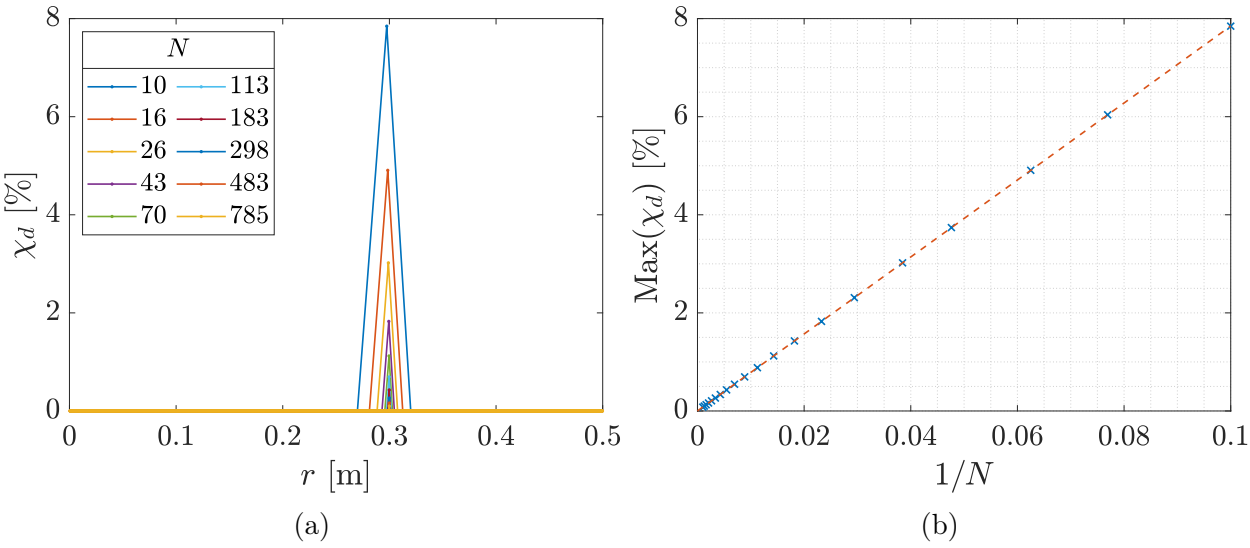

(a) (b)

Figure 9: Divergence and free charges study by means of the difference χ_d described in the text. (a) Verification of Gauss' law by plotting χ_d over the course of the simulation; (b) Convergence study of the maximum absolute value of χ_d for 20 simulations and $N_1 = N_2 \in [10, 1000]$.

A fit has been drawn through the points to better show the fact that the trend of the graph is linear. This implies that the order of convergence is of 1. This is different to the previous cases, and may be due to the discontinuity of the divergence of the electric displacement at $r = b$. However, the linear regression seems to indicate that the error does to tend to vanish as N tends to infinity, confirming that the error in Gauss' law is purely numerical.

Bound charges The bound charge density ρ_b within the configuration can be calculated as

$$\rho_b = \varepsilon_0 \nabla \cdot \vec{E} - \nabla \cdot \vec{D}\,, \tag{45}$$

and is thus plotted in Figure 10, for varying numbers of intervals N.

It can be seen that, as predicted by the analytic calculations, the bound charge density is zero everywhere except at $r = b$, where a sharp peak occurs. It should be noted that the height of this peak augments as the number of intervals N increases. Similarly, the width of the peak diminishes when N grows. This is to be expected, as the analytic calculations predict a non-zero total bound charge $Q_{b,tot}$ (see equation (41)), yet the bound charge density is analytically zero everywhere except at $r = b$. This can be explained physically by the accumulation of bound charges on the surface at the interface of the two different materials, which mathematically can be translated as a vertical asymptote for the bound charge density ρ_b at $r = b$. As a matter of fact, the density ρ_b is per unit volume, whereas the configuration tends towards a surface density at $r = b$. This explains physically why, even though ρ_b is unbounded at $r = b$, the total bound charge is finite. The total bound charge, which has been analytically calculated in equation (41), giving $Q_{b,ana}/L_z = 1.19475 \times 10^{-8}$ C/m, is

numerically computed using the the trapezium rule,

$$Q_{b,tot} = \int_V \rho_b \mathrm{d}V \approx \pi \sum_{i=1}^{N} h_i (r_i \rho_b(r_i) + r_{i+1}\rho_b(r_{i+1}))\,, \tag{46}$$

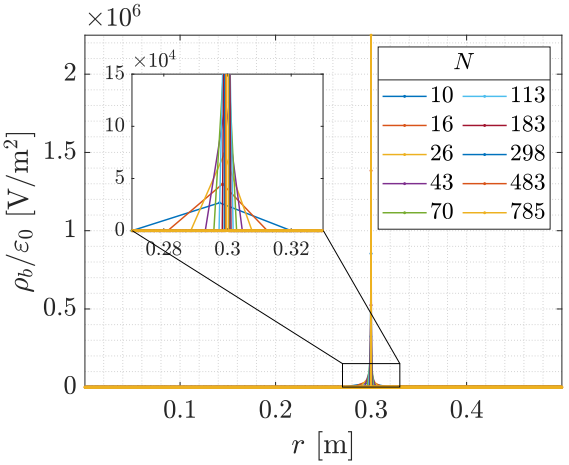

Figure 10: Bound charge density profiles obtained for ten numbers of steps $N = N_1$ taken and a mesh factor of 1.

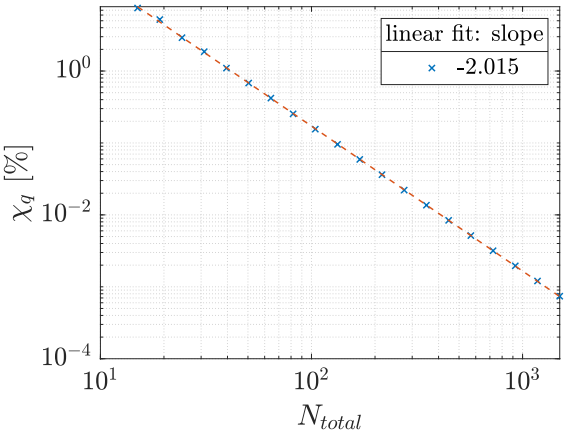

Figure 11: Convergence study on χ_q, with 20 simulations and a mesh factor of 0.5 ($N_1 = 0.5N_2$).

A convergence study was then undertaken to verify that this numerical approximation does tend towards the analytic solution as the number of intervals N increases. This is shown in Figure 11, where the relative error on the total charge per unit length, noted

$$\chi_q = \left| \frac{Q_{b,ana} - Q_{b,num}}{Q_{b,ana}} \right| \times 100\,, \tag{47}$$

is plotted against increasing values of the total number of intervals N_{total} on a loglog scale. A linear regression has been plotted to verify the order of convergence, which is still 2, as in the trivial case.

Different free charge density and relative permitivitty We now choose a different configuration, with

$$\rho_f(r)/\varepsilon_0 = \begin{cases} a_0 e^{-\left(\frac{r}{b}\right)^2} & \text{if } 0 \leq r < b \\ \frac{a_0}{\ln\left(\frac{r}{R}\right)} & \text{if } b \leq r \leq R \end{cases}, \tag{48}$$

and

$$\varepsilon_r(r) = \begin{cases} \arctan\left[\left(\frac{r}{b}\right)^2\right] & \text{if } 0 \leq r < b \\ \frac{1}{1+\left(\frac{r}{R}\right)^5} & \text{if } b \leq r \leq R \end{cases}, \tag{49}$$

which are clearly conditions for which an analytic solution is impossible in a closed form. The importance of a numerical method can thus be appreciated. The free charge density and the relative permitivitty are shown in Figure 12.

The simulation was thus executed for different numbers of intervals N, and the electric field and potential have been plotted. This is shown in Figures 13a and 13b. The resulting

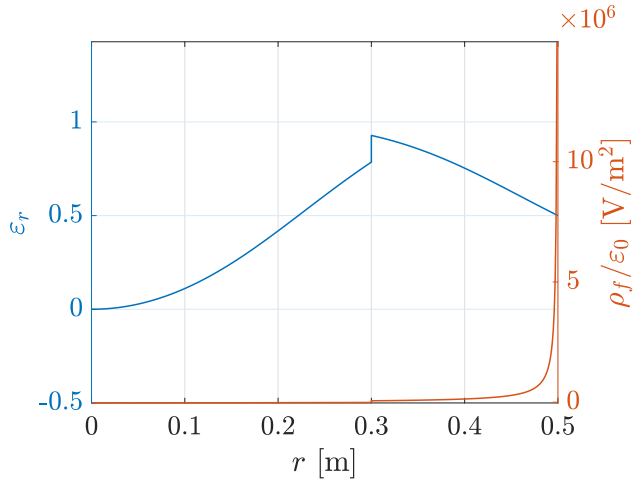

Figure 12: Free charges density and relative permittivity profiles chosen.

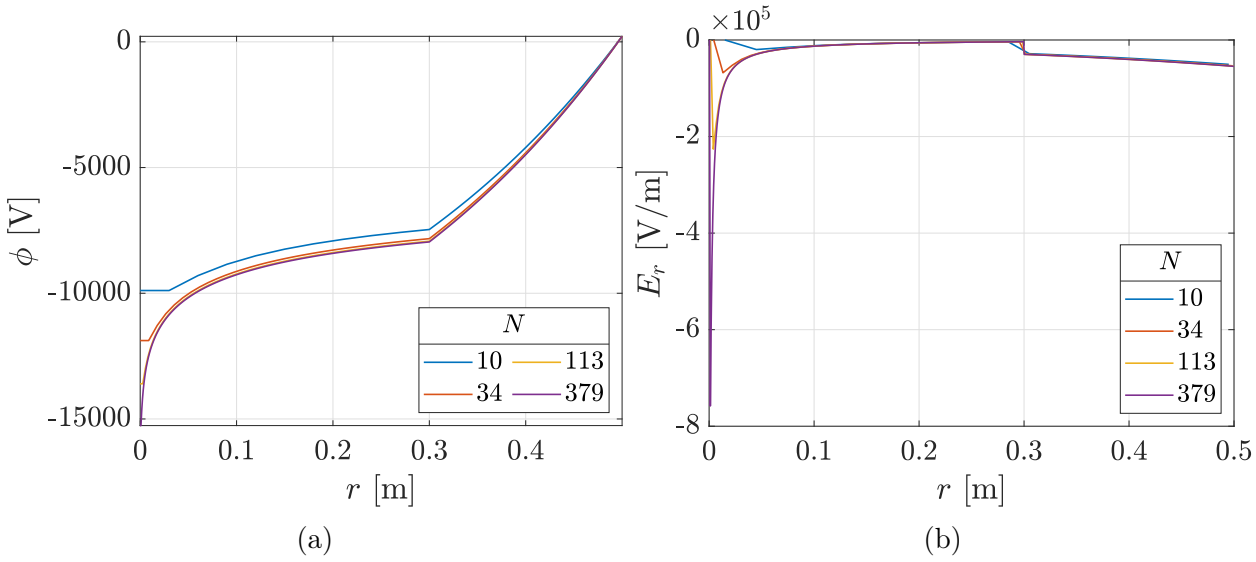

Figure 13: Potential (a) and electric field (b) obtained for different numbers of steps with the new free charge density and relative permittivity profiles shown in Fig.12. The potential is continuous across the whole domain as expected. The change in the definition of the two quantities is clearly visible at $r = b$

electric potential is mostly negative, commencing at approximately $\phi(0) \approx -15000$ V, and seems to increase as the radial distance increases. It should be noted, that as expected, the potential is still continuous at $r = b$ despite the discontinuity of the free charge density and the permitivitty. On the other hand, the electric field, the electric field is negative throughout, the cylinder, and seems to augment rapidly at first, then proceeds to tail off towards the exterior of the cylinder. The electric field has a discontinuity at $r = b$, as is to be expected.

Mixed trapezium midpoint method As seen in equation (11), the numerical approximation of the integrals calculated during this exercise has been implented with a parameter

p which controls the weight given to the method used: either the trapezium method $p = 1$ or the midpoint method $p = 0$. To study the optimal value of p necessary to obtain the maximal order of convergence, a simulation was executed with several convergence studies, such as the one shown in Figure 7, each for a different value of p. The orders of convergence (given by the absolute value of the slope of the best fit on a loglog plot of the error versus the number of intervals) was then plotted as a function of p. This has been shown in Figure 14b. It can be seen that the order of convergence does in fact vary slightly with p, which

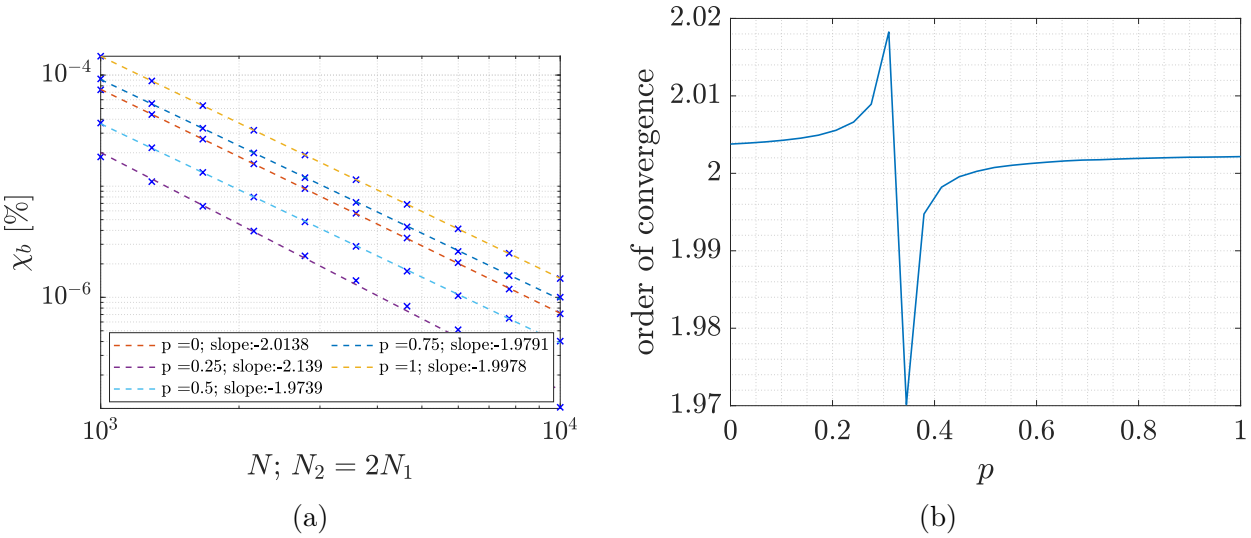

Figure 14: Qualitative and quantitative study of the impact of the parameter p on the order of convergence to the relative error χ_b of the simulation. (a) Orders of convergence obtained for different values of p; (b) Plot of the order of convergence obtained as a function of value for p used, for 30 different values in $[0, 1]$.

implies that there is an optimal method (somewhere between trapezium and midpoint), at least in the case of this exercise. The maximum of the order of convergence can be observed at $p = 0.3103$, where the order of convergence is 2.018, while the minimum lies at $p = 0.3448$, with an order of convergence of 1.97. However, globally, the order of convergence still remains at approximately 2.

4 Conclusion

This study allowed to solve numerically the laws of electrostatics in a cylinder with variable dielectric and free charges. The trivial computations that have first been carried out gave us the means to verify the validity of the equations obtained through variational analysis and Galerkin's method. The non-trivial case addressed then showcased the prioritisation of different spatial intervals, as well as the behaviour of the numerical solutions obtained in comparison to the analytic solutions derived. Gauss' law has been verified and the bound charges within the configuration calculated. Simulations have then been conducted with a different free charge density and relative permittivity. The continuity of the electric potential across all the domain was verified. Finally, the value of the parameter p used in the mixed trapezium and midpoint method has been varied to showcase which values yield respectively

the maximal and minimal orders of convergence of the relative error on the analytic potential at $r = b$.

References

[1] L. Villard and C. Sommariva, 'Physique Numérique II – Notes de cours', p.92. 2021, [Online]. Available: `https://moodle.epfl.ch/mod/resource/view.php?id=10257`.